

# Radiatively driven downdrafts and redshifts in transition region lines

## II. Exploring the parameter space

F. Reale, G. Peres, and S. Serio

Istituto e Osservatorio Astronomico G. S. Vaiana, Palazzo dei Normanni, I-90134 Palermo, Italy  
(e-mail: reale@oapa.astropa.unipa.it, peres@oapa.astropa.unipa.it, serio@oapa.astropa.unipa.it)

Received 25 March 1996 / Accepted 27 June 1996

**Abstract.** We address the hypothesis that downdrafts driven by radiatively-cooling condensations in the solar transition region are able to produce significant redshifts in UV lines as frequently observed on the solar disk and, more recently, on other stars. In a first paper, significant redshifted line components at several km/s have been found from modeling the evolution of an isobaric perturbation twice as dense as the unperturbed atmosphere, almost as large as the thickness of the transition region of an active region loop, and with central temperature higher than the formation temperature of the UV lines. In the present work we show the results of an extensive exploration of the space of the important parameters controlling the evolution of isobaric perturbations: density contrast ( $\delta$ ), dimensions, and ambient pressure. The center of most of the perturbations is placed where the temperature of the unperturbed medium is  $T_0 = 4.5 \cdot 10^5$  K, but higher temperatures do not lead to substantially different results. From the hydrodynamic evolution we synthesize the line flux and effective speed along the line of sight, and examine the distribution of the most intense Doppler-shifted components. In a wide region of the parameter space ( $\delta > 0.5$ , dimensions of the order of the thickness of the transition region) we find redshifted components at speeds of several km/s for ambient pressure values ranging from those typical of quiet Sun to active regions. The assumption of isotropic thermal conduction, or, alternatively, of 1-D hydrodynamics, i.e. mimicking the effect of strong magnetic fields, lead to qualitatively similar results. Our calculations suggest also that redshifts may occur more easily in the higher pressure plasma, typical of active regions, in general consistency to observations.

**Key words:** stars: atmospheres – Sun: transition region – stars: UV radiation

### 1. Introduction

In this study we investigate the hypothesis that radiatively cooling condensations in the chromosphere-corona transition region can produce intense redshifted UV lines, similar to those frequently observed on the Sun, and also on other stars. In this scenario the redshifted emission is caused by downflows in the transition region, driven both by thermal effects and by gravity.

A previous analysis (Reale, Serio & Peres 1994, hereafter RSP) has shown that isobaric perturbations subject to the competing action of thermal conduction and radiative losses in a gravitationally stratified and initially isothermal atmosphere can lead to a thermal instability and produce significant downflows, when they are significantly denser than the unperturbed medium, and of size comparable to the thickness of the transition region.

While the origin of the perturbations has not been studied in detail, it appears unlikely that they could be due to purely hydrodynamic effects (Hansteen 1993). Non linear MHD waves, which may determine strong local deformations of the magnetic field, might be invoked in their generation. Hansteen, Maltby and Malagoli (1996) do indeed propose this kind of mechanism to produce disturbances in corona which, propagating downward, may drive the redshifts. Instead, in our approach, even initially stationary disturbances contribute to the redshifts.

In the first paper of the present series (Reale, Peres & Serio 1996, hereafter Paper I), we have shown that a spherical isobaric condensation twice as dense as the unperturbed medium, and extending in height over most of the transition region of a solar active region, produces redshifted components of UV lines much more intense than static and blueshifted components. The redshift values are generally consistent with the observed ones. In that paper we have modelled the perturbation inside a thermally stratified solar atmosphere with a two-dimensional hydrodynamic code (see Reale 1995 for details) and we have synthesized the line fluxes and effective speeds along the line of sight from the computed density, temperature and velocity

evolution. We have discussed the assumptions and techniques used in our calculations, as well as the methods adopted in the analysis of the results. We found intense redshifted emission between 5 and 10 km/s in all of the four UV lines considered (Si IV 1402.77 Å, C IV 1548.20 Å, O IV 1401.16 Å and O V 1371.30 Å). Similar results have been obtained when thermal conduction is active only along the vertical direction (to mimic the effects of magnetic fields). Higher redshifts have been found in a purely one-dimensional description.

Along the same line of thought, here we show that significant redshifts in UV lines are likely to be caused by a variety of perturbations in typical solar ambient conditions. To this end we explore the space of the control parameters. In particular we investigate the influence of the ambient pressure, and of the initial size, contrast and location of the perturbations, on their physical evolution, and on the synthesized line emission. In particular we aim at determining the range of parameters for which intense redshifted emission is obtained, the values of the typical redshifts and their dependence on the ambient pressure.

This paper is organized as follows: in Sect. 2 we describe the parameters space explored; in Sect. 3 we illustrate the results, describing both the evolution of the plasma and the synthesized line emission; in Sect. 4 we discuss the results.

## 2. The control parameters space

In Paper I we have defined four parameters which control the evolution of spherical isobaric perturbations in a gravitationally and thermally stratified atmosphere: i) the plasma pressure  $p$  at the base of the transition region, ii) the temperature  $T_0$  of the unperturbed atmosphere at the center of the perturbation, iii) the initial density contrast of the perturbation  $\delta = (\rho - \rho_0)/\rho_0$ , iv) the radius  $R$  of the perturbation. A relevant quantity, frequently discussed in the following, is the ratio  $R/h_0$ , where  $h_0$  is the height of the center of the perturbation above the base of the unperturbed transition region.

In the present work we extensively explore a region of this parameter space approximately centered on the reference model of Paper I – results for this model are summarized in Sect. 3) – and representative of the wide spectrum of conditions likely to be present in the solar atmosphere. The evolution of each model perturbation is computed as in Paper I (see Reale 1995 for more details on the numerical techniques), by solving numerically the two-dimensional time-dependent hydrodynamic equations in a straight vertical cylinder with height  $z = z_{max}$  and radius  $r = r_{max}$  as a simplified model for one leg of a coronal loop. The bottom of the cylinder  $z = 0$  represents the vertically rising chromospheric foot of the coronal loop, where reflecting boundary conditions are assumed, and the top of the cylinder  $z = z_{max}$ , way above the region affected by the perturbation, is the highest point of the loop; there the horizontal loop structure is mimicked by vanishing gravity and velocity, and vanishing gradients of density and temperature. The perturbations, however, occur and evolve in a very thin layer inside the transition region. Also the horizontal distance of the outer

boundary of the cylinder  $r = r_{max}$  is taken much larger than the perturbation radius.

The initial vertical stratification is borrowed from loop atmospheres, determined according to the hydrostatic loop models of Serio et al. (1981), with base pressure  $p = 0.1, 3$  and  $10$  dyn cm<sup>-2</sup>, i.e. ranging from the quiet Sun to active regions.

A typical initial configuration of our model computations, the reference model described in Paper I with  $p = 3$  dyn cm<sup>-2</sup>, is shown in Fig. 1. The initial isobaric perturbation is the depression visible in the temperature vertical distribution (Fig. 1a), and the prominence in the density distribution (Fig. 1b). Both these panels are an enlargement of the whole atmosphere shown in Fig. 1d. The spherical perturbation geometry is shown in the picture of the initial density contrast  $\delta$  (Fig. 1c), which includes a small region around the perturbation. The horizontal outer boundary, not visible in the figure, is placed at  $R_{max} = 200$  km from the central axis.

As clear from Fig. 1, we study perturbations extending over a large fraction of the transition region. In particular the radius of the perturbations is selected in a range  $0.25 < R_0/h_0 < 1$ , where  $h_0 \approx 1.4 \cdot 10^8, 4 \cdot 10^6, 1.1 \cdot 10^6$  cm for the three respective pressure values when  $T_0 = 4.5 \cdot 10^5$  K. Therefore the largest condensations ( $R/h_0 = 1$ ) extend over most of the transition region, down to the top of the chromosphere. The solar perturbations considered here, although candidate to produce spectral signatures, subtend at the earth much less than one arcsec, except in low pressure regions, and cannot be resolved with present day instruments. Perturbations with  $R/h_0 < 0.25$  are of no interest here, since, as shown in Paper I, they would be disrupted very rapidly by thermal conduction, well before they produce any emission signature.

The spacing of the numerical grids used in our calculations has been chosen so that the radius of the initial perturbation covers at least 15 grid cells along each direction. We remind that the grid is not equispaced along the  $z$ -direction, in order to follow the steep gradients of the transition region, while being equispaced along  $r$  in the region around the perturbation.

We consider perturbations with positive initial density contrast in the range  $0.1 \leq \delta \leq 3$ , i.e. from quasi-linear to very non-linear regime. The weakest perturbations ( $\delta \approx 0.1$ ) are thermally stable (cf. RSP), whatever their size, and are disrupted before giving any observable signature. On the other hand, the most intense perturbations ( $\delta = 3$ ) have core temperature already below the temperature of formation of the representative UV lines we have selected, and therefore do not contribute to the line shifts. We will not discuss perturbations with negative density contrast ( $\delta < 0$ ). In a test computation, assuming a perturbation identical to the reference model but with  $\delta = -0.5$ , we have found that such perturbation is rapidly cancelled by thermal conduction, well before the development of any observable feature.

Most of the perturbations are at  $T_0 = 4.5 \cdot 10^5$  K. This temperature is higher than the formation temperatures of the lines of interest, and is typical of the middle layers of the transition region. We do not consider lower values of  $T_0$ , because intense perturbations, i.e. the best candidate to give observable effects,

## Reference Model

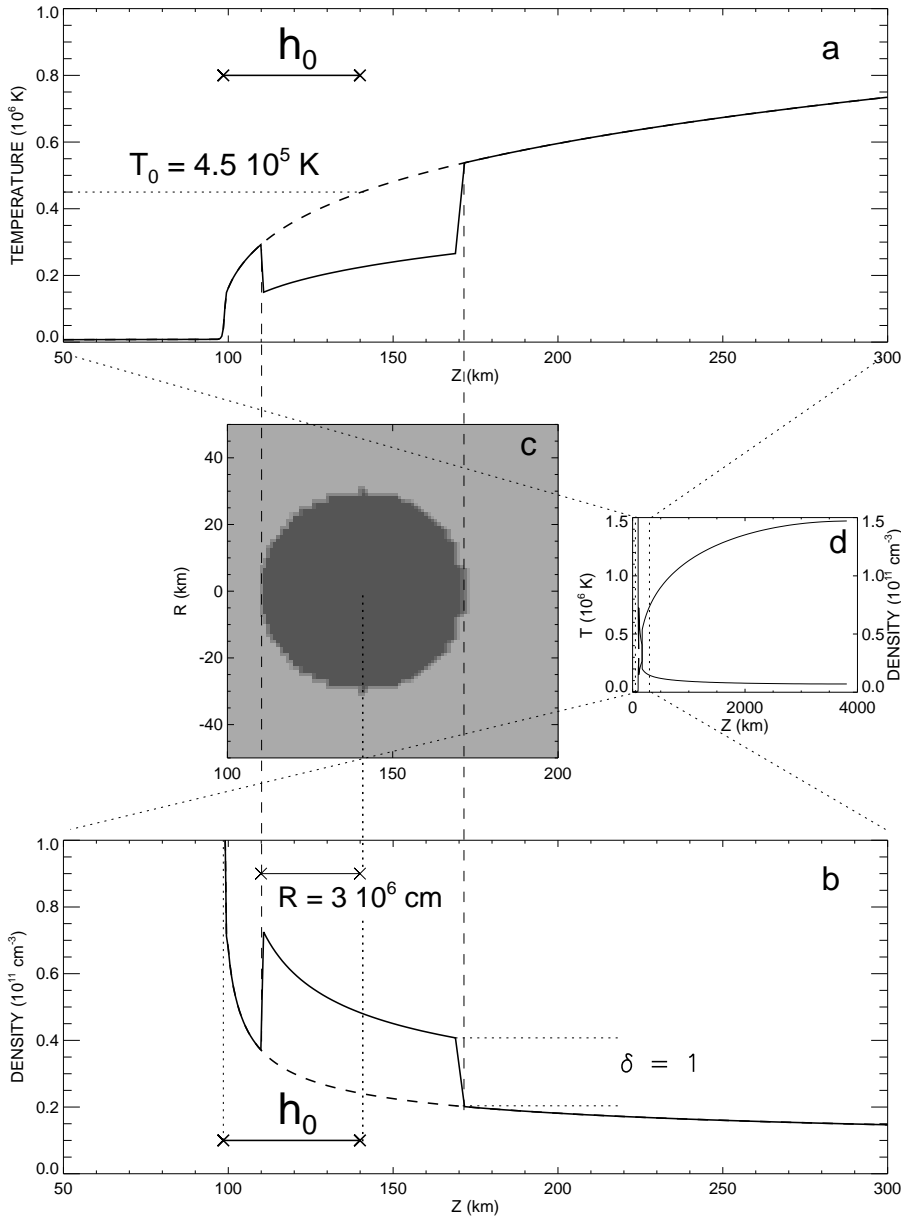


**Fig. 1a–d.** Initial configuration of the two-dimensional hydrodynamic evolution of the reference model (cf. model 11 in Table 1); the geometry is cylindrical with coordinates  $r, z$ . Panels **a** and **b** show the temperature and density distributions along the vertical  $z$  axis ( $r = 0$ ), across the center of the perturbation (solid lines), along with the unperturbed distributions (dashed line). Panel **c** shows a picture of the initial density contrast  $\delta$ . Panels **a**, **b** and **c** show a limited region of the whole computational domain, in order to illustrate better the perturbation, whose radius is smaller than the thickness of the transition region. Panel **d** shows the density and temperature distributions along the vertical  $z$  direction. Some relevant quantities are indicated ( $T_0$ ,  $R$ ,  $h_0$ ,  $\delta$ , see text for further details).

would evolve permanently below the line formation temperature. We instead study some perturbations with  $T_0$  up to  $6.5 \cdot 10^5$  K, which corresponds to a larger  $h_0$ . For higher values of  $T_0$  thermal conduction becomes extremely efficient in attenuating the thermal gradients, and in disrupting the perturbations.

Most models are studied assuming isotropic thermal conduction and fully 2-D hydrodynamics in cylindrical coordinates; the effect of deviations from these physical assumptions have been examined in Paper I. In order to evaluate the effect of ordered magnetic fields, we study the parameter subspace with pressure  $p = 3 \text{ dyn cm}^{-2}$ , typical of active regions where magnetic fields are stronger, with a one-dimensional treatment, both for the hydrodynamics and thermal transport.

We present the results and compute the line emission flux and effective speed as in Paper I. We first compute the line flux

$F(r, t)$  integrated along the the line of sight (in the direction of the solar disk center):

$$F(r, t) = \int n^2(r, z, t) G(T(r, z, t)) dz \quad (1)$$

where  $G(T)$  is the plasma emissivity per unit emission measure (Landini & Monsignori Fossi 1990) in each of the four UV lines Si IV (1402.77 Å), C IV (1548.20 Å), O IV (1401.16 Å), O V (1371.30 Å), with temperature of maximum emissivity, respectively of  $7 \cdot 10^4$  K,  $10^5$  K,  $1.4 \cdot 10^5$  K,  $2.4 \cdot 10^5$  K; analogously, we compute the effective vertical speed  $v_{ze}(r, t)$ , i.e. the average velocity along the line of sight weighted by emission in the line:

$$v_{ze}(r, t) = \frac{\int v_z(r, z, t) n^2(r, z, t) G(T(r, z, t)) dz}{\int n^2(r, z, t) G(T(r, z, t)) dz} \quad (2)$$

**Table 1.** parameters and results of 2-D models

#	p	$h_0$	R	$\delta$	$\delta_{max}$	$v_{max}$	SiIV		CIV		OIV		OV	
(1)	dyn/cm <sup>2</sup>	10 <sup>6</sup> cm	10 <sup>6</sup> cm	(5)	(6)	km/s	$v_F$	$F_{max}/F_0$	$v_F$	$F_{max}/F_0$	$v_F$	$F_{max}/F_0$	$v_F$	$F_{max}/F_0$
(1)	(2)	(3)	(4)	(5)	(6)	(7)	(8)	(9)	(10)	(11)	(12)	(13)	(14)	(15)
1	3	4	1	0.5	0.7	14	0.26	1.1	-1.6	1.2	0.33	1.1	1.2	1.0
2 <sup>a</sup>	3	4	1	1	1.7	17	0.24	1.0	-1.8	1.1	0.089	1.0	2.1	1.1
3	3	4	1	2	3.4	24	0.28	1.1	0.58	1.1	2.2	3.7	2.7	3.1
4	3	4	1	3	4.9	23	3.5	2.0	5.2	1.6	3.9	6.2	4.6	2.1
5	3	4	2	0.5	0.8	10	1.3	1.2	-0.95	1.1	1.5	1.1	4.0	1.6
6 <sup>a</sup>	3	4	2	1	1.8	12	0.96	1.1	-1.4	1.2	6.0	3.0	6.4	4.1
7	3	4	2	2	4.3	12	5.3	8.2	7.6	20	5.6	7.9	4.6	3.1
8	3	4	2	3	23	12	3.8	20	8.4	52	5.5	6.3	3.6	2.8
9	3	4	3	0.3	0.5	7.7	1.2	1.1	-1.2	1.1	3.1	1.5	5.0	1.9
10 <sup>a</sup>	3	4	3	0.5	1.2	11	1.5	1.6	1.9	1.4	5.7	2.5	7.3	3.3
11 <sup>b</sup>	3	4	3	1	10	16	5.0	11	5.5	9.6	7.9	8.3	7.5	6.1
12 <sup>a</sup>	3	4	3	2	52	17	5.6	23	8.9	32	8.9	14	5.1	2.9
13	3	4	3	3	87	17	8.2	55	8.4	29	5.4	6.3	4.9	2.7
14	3	4	4	0.1	0.3	2.9	0.44	1.1	-1.4	1.1	1.4	1.3	2.2	1.2
15	3	4	4	0.3	1.2	8.0	2.1	1.7	1.9	1.5	5.0	2.2	6.1	2.1
16	3	4	4	0.5	3.1	11	3.7	2.0	3.2	3.0	7.3	3.8	8.4	3.1
17 <sup>a</sup>	3	4	4	1	19	16	8.6	17	5.3	22	7.8	5.3	8.6	4.5
18 <sup>a</sup>	3	4	4	2	46	22	10	48	5.7	10	6.7	5.7	6.1	2.3
19	3	4	4	3	180	24	11	41	8.6	5.6	5.1	4.6	6.0	2.0
20 <sup>c</sup>	3	12	9	1	14	18	4.7	3.7	5.5	8.3	6.8	4.1	9.6	8.4
21	0.1	140	50	0.5	0.7	10	0.48	1.0	0.69	1.0	1.6	1.1	2.5	1.2
22	0.1	140	50	1	1.4	13	0.95	1.0	0.88	1.1	3.0	1.1	4.9	1.9
23	0.1	140	50	2	3.2	13	1.1	1.2	3.0	2.0	6.1	4.3	6.2	3.3
24	0.1	140	50	3	5.1	11	5.9	5.7	6.4	12	6.4	4.7	5.6	3.0
25	0.1	140	100	0.5	2.1	8.2	1.6	1.4	2.2	1.4	4.8	1.8	6.5	2.2
26 <sup>a</sup>	0.1	140	100	1	3.4	11	2.6	2.1	4.2	2.1	7.6	3.7	7.5	3.2
27	0.1	140	100	2	5.7	17	9.9	13	8.1	10	8.6	4.4	7.3	2.1
28	0.1	140	100	3	19	27	11	19	9.8	10	7.6	3.5	6.4	1.8
29	0.1	140	140	0.5	4.8	13	4.7	2.9	7.0	2.6	9.5	2.7	11	2.4
30	0.1	140	140	1	9.2	18	9.0	6.9	14	6.2	14	4.4	9.1	1.9
31	0.1	140	140	2	18	30	19	15	13	7.3	12	3.3	7.8	1.8
32	0.1	140	140	3	30	40	16	16	14	8.4	9.8	3.3	7.0	1.7
33 <sup>a</sup>	10	1.1	0.85	1	6.5	15	3.7	3.3	4.9	7.9	8.0	8.2	7.7	6.3

Notes to Tabel 1:

**Col.(2):** pressure at the base of the transition region.**Col.(3):** vertical distance of the center of the perturbation from the base of the transition region.**Col.(4):** initial radius of the perturbation (10<sup>6</sup> cm).**Col.(5):** initial density contrast of the perturbation  $((\rho - \rho_0)/\rho_0)$ .**Col.(6):** maximum density contrast during the evolution.**Col.(7):** maximum vertical downward speed of the plasma.**Col.(8,10,12,14):** effective vertical speed (positive downwards, km/s) at which plasma emits with maximum intensity in the line indicated.**Col.(9,11,13,15):** maximum flux contrast with respect to the static component.<sup>a</sup> Cases explicitly mentioned in the text.<sup>b</sup> Reference model.<sup>c</sup>  $T_0 = 6.5 \cdot 10^5$  K (for all the others  $T_0 = 4.5 \cdot 10^5$  K).

In this work we discuss the generation of Doppler shifts referring to individual perturbations in the transition region and without making any assumption on the spectrum of the perturbations. Therefore, as we have done in Paper I, we will discuss the flux distribution of line components at different Doppler shifts, corresponding to different velocities  $v_{ze}$ , per unit time and unit area. To this purpose we have divided the relevant range of

effective speeds into bins, of central value  $\bar{v}_{ze}$  and amplitude typically  $\Delta v \sim 1$  km/s, and computed the weighted average flux in each speed bin by summing up the flux contributions of all the elementary cylindrical shells and the time intervals in which the effective speed is in the range  $\bar{v}_{ze} \pm \Delta v/2$ :

$$F_{avg}(\bar{v}_{ze}) = \frac{\sum_{i,j} 2\pi r_i F(r_i, t_j) \Delta r_i \Delta t_j}{\sum_{i,j} 2\pi r_i \Delta r_i \Delta t_j} \quad (3)$$

In the analysis reported in Sect. 3, we will consider the effective velocity ( $v_F$ ) of the most intense flux component ( $F_{max}$ ) as an indicative Doppler shift. In the reference model, this speed is also the highest effective speed of the distribution, because the flux distribution monotonically increases with increasing redshifts. In general this may not be case, especially for more intense and large perturbations, but we will not take into account the presence of such higher speed components.

### 3. Results

#### 3.1. The role of the control parameters

The parameters of the 2-D models we consider here are listed in Table 1, where we provide the parameters  $p_0$ ,  $h_0$ ,  $R$  and  $\delta$  (columns 2-5), the maximum plasma density contrast (6) and maximum downward speed (7) reached during the evolution, and in columns 8 to 15, for each of the four lines considered, the effective speed  $v_{ze} = v_F$  of the most luminous Doppler-shifted component  $F_{avg}(v_F) = F_{max}$ , and the ratio  $F_{max}/F_0$  of the maximum flux to the average flux from the static component. The parameters in columns 5 and 6 are useful to characterize the evolution of the perturbations, and those in columns 7-14, although not directly comparable to measured quantities, provide an indication of the characteristic Doppler shifts.

In Paper I we have described in detail the results obtained for the specific model of an isobaric condensation evolving inside a vertically stratified atmosphere. We summarize now its crucial features and then discuss how they change with the control parameters.

Consider the development of a condensation of radius  $R = 3 \cdot 10^6$  cm, with density contrast  $\delta = 1$  and center at height  $h_0 = 4 \cdot 10^6$  cm from the base of the transition region (cf. Table 1 case 11), where the temperature of the unperturbed medium is  $T_0 = 4.5 \cdot 10^5$  K. The vertical stratification is typical of an active region loop with base pressure  $3 \text{ dyn cm}^{-2}$ . Since the perturbation is assumed isobaric, the temperature in the condensation is considerably lower than the undisturbed atmosphere outside.

The evolution is first characterized by a rapid attenuation of the temperature contrast at the top of the perturbation, where the outside temperature is higher, and thermal conduction more efficient. The accompanying overpressure drives an outward radial motion reaching  $v \approx 16$  km/s, at  $t = 0.2$  s. Thermal conduction is less efficient in the lower half of the perturbation, where plasma cools down radiatively, and the density contrast increases monotonically during the first 3 s, up to  $\delta \approx 10$ . At the same time the region of highest density contrast drifts downwards and reaches the base of the transition region at  $t \approx 2.6$  s. After  $t \sim 0.8$  s most of the plasma motion is downwards ( $v > 10$  km/s) and located in the region with high  $\delta$ . After  $t = 2.6$  s, the plasma speed rapidly decreases to  $v \sim 3$  km/s, and the condensation gradually disappears.

In Paper I we have also discussed the characteristics of the emitted flux and effective speed due to this evolution in four selected UV lines. We have found that the plasma in the downward drifting part of the perturbation emits more intensely than

the surrounding “static” region in all the lines, yielding effective speeds along the line of sight of several km/s. When we have considered the flux distribution of the line components at different effective speeds (cf. Eq. 3), we have found that the fastest downward moving components are also the most intensely emitting ones – with flux between 5 and 10 times more intense than the static component – while upward moving components are much weaker and slower. This suggests that significant redshifts in the four UV lines may be produced during the evolution of the perturbed atmosphere.

In the following we discuss the role of the control parameters. In Figs. 2–5 we show, for each model discussed, the flux distribution of the Doppler-shifted components in the four UV lines, which can be compared to that of the reference model.

##### 3.1.1. Initial density contrast

**Small:** For  $\delta = 0.5$  (model 10 in Table 1), the perturbation radiates less, and is attenuated more efficiently by thermal conduction with respect to the reference model. The evolution is globally similar to that of the reference model, but the flow motions are slower ( $v_{max} \approx 12$  km/s), and the density contrast never increases significantly ( $\delta_{max} \approx 1.2$ ). As shown in Fig. 2, this more stable evolution produces downward moving components at speeds similar to the reference model in the OV line, although at lower flux contrasts. In the other cooler lines, redshifted components are slow and weak ( $v_{ze} < 5$  km/s,  $F_{max}/F_0 < 3$ ).

**Large:** For  $\delta = 2$  (model 12 in Table 1), the perturbation radiates and cools down very efficiently, and its core becomes thermally unstable. The density contrast first gets to a very high value ( $\delta \approx 52$  at  $t = 2$  s) and then slowly decreases. Plasma moves at speeds higher (+20%) than in the reference model. A rapidly cooling region forms below the perturbation, because the heat flux normally conducted in the unperturbed atmosphere is now much less than that required for energy balance. In the meantime, the dense core falls down at an average speed of  $\sim 5$  km/s, and reaches the base of the transition region at  $t \approx 3$  s. At that level it takes about 6 s to become a flat, thin, and practically static, disk.

As shown in Fig. 2, this stronger perturbation produces higher redshifts and more intense redshifted components in the three cooler lines, SiIV, CIV, OIV, but not in the OV line. Indeed, given the high initial contrast of density and temperature, most of the cooling and collapsing plasma is cooler, already from the beginning, than the temperature of maximum emissivity of this line, but not of the other “cooler” lines. In fact, the same perturbation but with  $\delta = 3$  produces less significant redshifts also in the OIV line, the second hottest one. In practice, more evident redshifts are produced by intense perturbations in cooler lines, and by weaker perturbations (but still with  $\delta \geq 1$ ) in hotter lines.

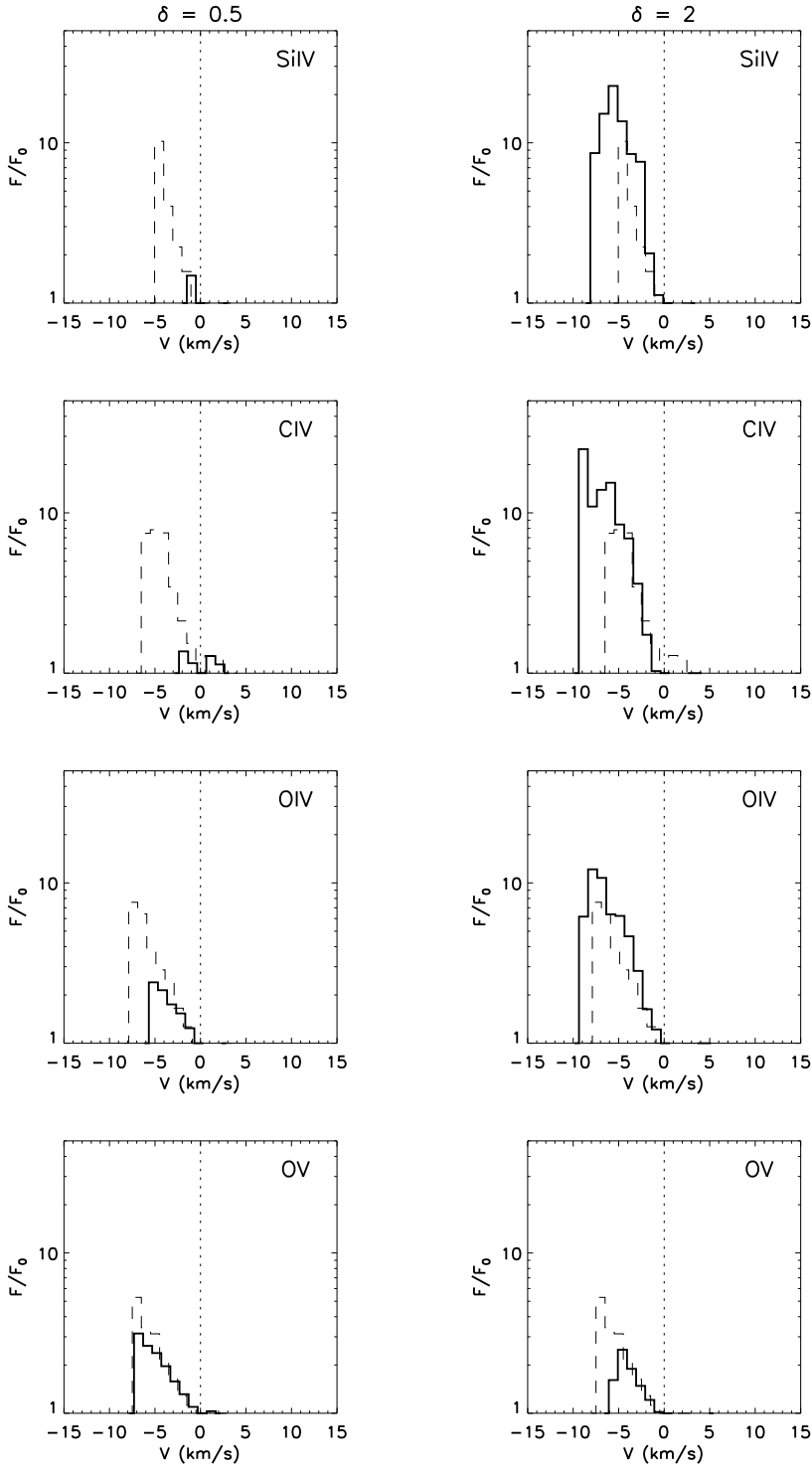


**Fig. 2.** Average emitted flux vs effective velocity in the four UV lines, in units of the average flux from the static components, for models differing from the reference model only for the initial density contrast ( $\delta$ ) (cf. Sect. 3.1.1). Results of the reference model are also shown for comparison (dashed lines).

### 3.1.2. Radius

**Small:** A perturbation of dimensions smaller than those of the reference model ( $R = 2 \cdot 10^6$  cm  $\approx 0.5 h_0$ , model 6 in Table 1) is attenuated more efficiently by thermal conduction. A fast flow expands isotropically from the center of the perturbation at the beginning of the evolution ( $v_{max} \approx 17$  km/s at  $t \approx 0.3$  s). The density contrast first increases mod-

erately ( $\delta \approx 1.8$  at  $t \approx 0.2$  s), and then decays rapidly:  $\delta_{max} \approx 0.5$  at  $t \approx 0.5$  s and  $\delta_{max} \approx 0.05$  at  $t \approx 5$  s. Such an evolution leads to significant redshifted components of the oxygen lines (Fig. 3), but to almost no Doppler shift in the two coolest lines.

**Large:** For  $R = 4 \cdot 10^6$  cm  $\approx h_0$  (model 17 in Table 1) the perturbation practically extends over the whole transition

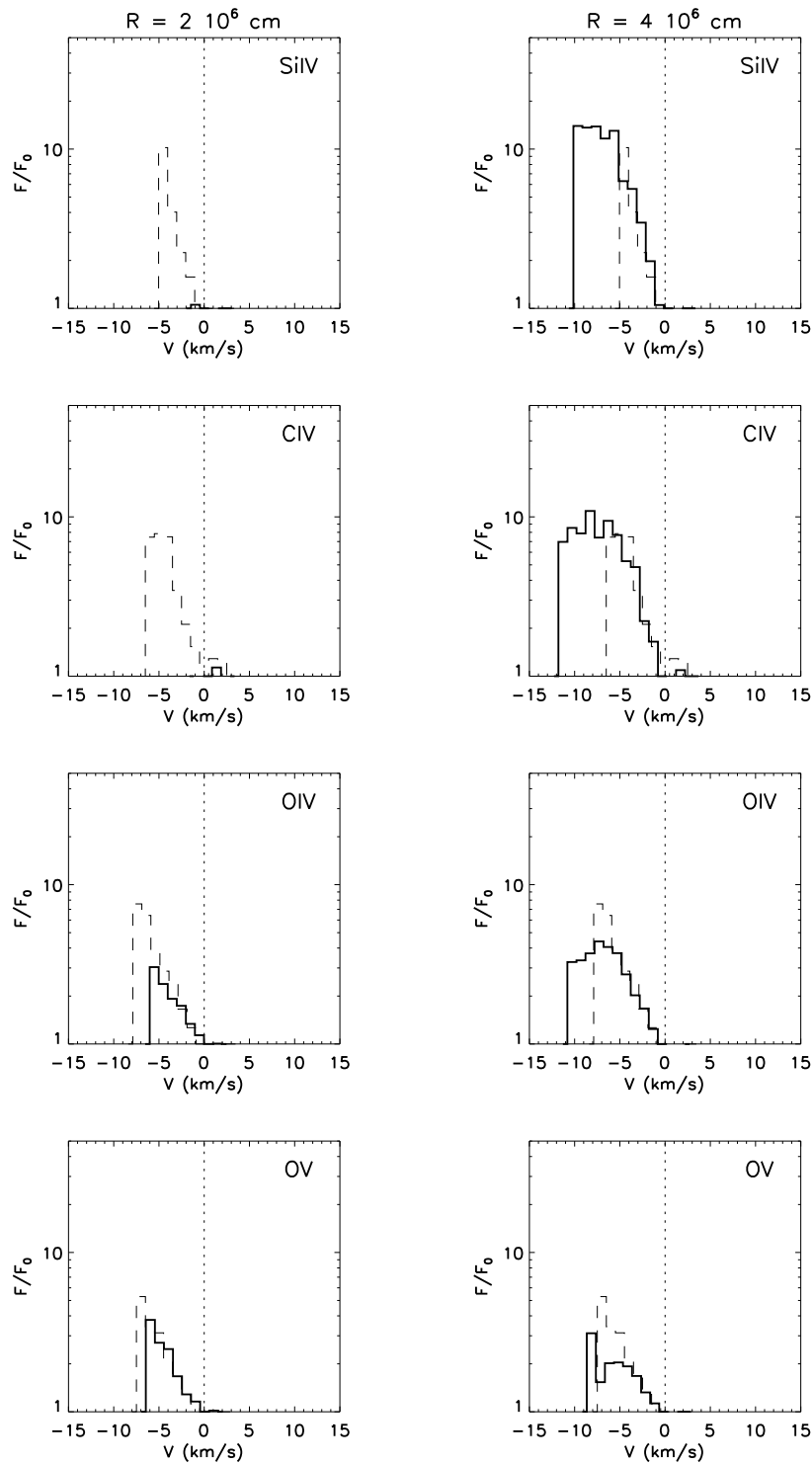


**Fig. 3.** Same as Fig. 2 for perturbations with different initial radius ( $R$ ) (cf. Sect. 3.1.2).

region below  $T_0$  and is more thermally unstable. In fact, the maximum density contrast is nearly doubled with respect to the reference model, but the densest part of the perturbation, located in its lowest part, falls across a smaller distance and reaches the base of the transition region sooner. Vertical motions are similar to those produced in the reference model and, as a result, all lines are characterized by intense redshifted components (Fig. 3), up to 11 - 12 km/s. In Si IV

line the maximum flux is 50% higher than in the reference model.

### 3.1.3. Temperature

We also analyze perturbations starting at a higher level, i.e. with a higher  $T_0$ . If we leave the radius  $R$  unchanged, the perturbation is rapidly cancelled by the higher thermal conduction. We will

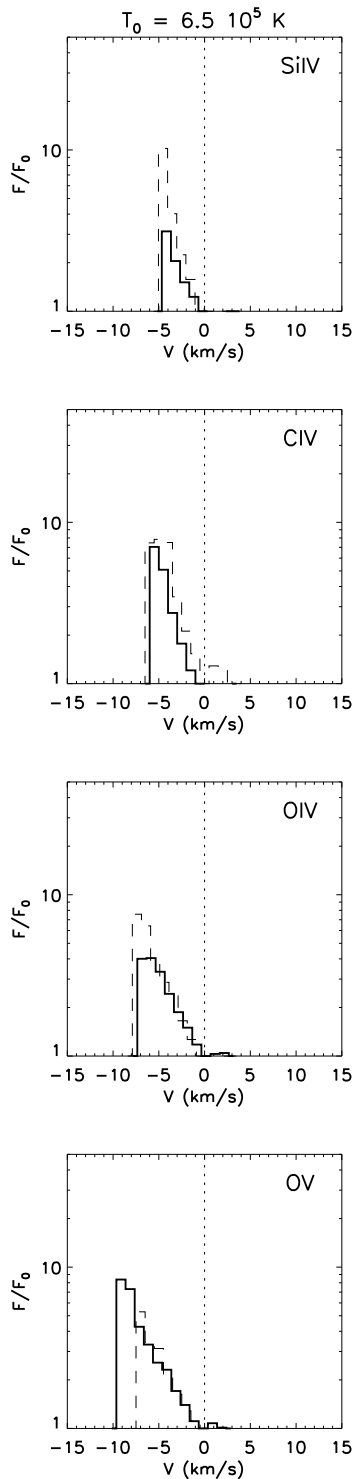


**Fig. 4.** Same as Fig. 2 for a perturbation with a different background temperature at its center ( $T_0$ ) (cf. Sect. 3.1.3).

instead discuss the case of a perturbation with  $T_0 = 6.5 \cdot 10^5$  K (model 20 in Table 1), and  $R = 9 \cdot 10^6$  cm i.e. three times larger than in the reference model. Since for  $T_0 = 6.5 \cdot 10^5$  K  $h_0 = 1.2 \cdot 10^7$  cm, this perturbation has the same ratio  $R/h_0 = 0.75$  as the reference model.

The evolution of this perturbation is slower than that of the reference one: the maximum density contrast, not much higher than the reference model, is reached in twice the time. The maximum flow speed is  $\approx 18$  km/s, at  $t \approx 0.7$  s, but is already  $< 10$  km/s after  $t = 1.4$  s. The core of the perturbation reaches the base after  $\sim 6$  s, 3 s later than in the reference model. In spite of the slower evolution, the line features are not significantly different (Fig. 4). In the O V line the maximum flux is slightly higher and at a slightly higher speed (+2 km/s). In the other lines we find similar speeds, but quite lower maximum fluxes with respect to the reference case.

### 3.1.4. Base pressure

The width of the transition region, as well as the scale lengths involved in the thermal stability of perturbations, varies inversely with the base pressure (cf. Paper I). Therefore, when we assume different pressures, we scale the perturbation size proportionally to the thickness of the transition region, i.e. we consider perturbations with the same  $R/h_0 = 0.75$ .

**Low:  $p = 0.1$  dyn cm $^{-2}$ .** The radius of the perturbation is  $R = 10^8$  cm (model 26 in Table 1), i.e. thirty times larger than the reference perturbation. Its evolution resembles that of the reference model but on a much longer time scale ( $\sim 60$  s), since larger distances are covered by plasma flows at comparable speeds<sup>1</sup>.

The perturbation is slightly more thermally stable and the flows are slower: the maximum density contrast and maximum speed are lower and occur much later ( $t \approx 18$  s, 6 times longer than in the reference model). On such long evolution times, we observe the formation of upward return flows, which, however, have negligible effects on line emission. As in the reference model, thermal conduction dominates the evolution, taking  $\sim 50$  s to dissipate the perturbation, and leaving thereafter only a static thin disk at the base of the transition region. Also at lower pressure we find that the heavy cool cores of very intense perturbations ( $\delta \geq 2$ , e.g. Model 23 in Table 1) are less controlled by thermal effects and fall down by gravity.

Because of this more stable evolution, which leads to lower density values, the maximum flux contrast in all lines (cf. Fig. 5) is significantly lower than in the reference model, a factor  $\sim 5$  in the two cooler lines and  $\sim 2$  in the two O lines. The maximum effective speed is lower in the Si IV and C IV lines.

**High:  $p = 10$  dyn cm $^{-2}$ .** The radius is  $R = 0.85 \cdot 10^6$  cm (model 33 in Table 1), i.e. 3 times smaller than in the reference case. The transition region is very thin, and the evo-

<sup>1</sup> The speed is dictated mainly by the local sound speed, which does not change, since the plasma temperature remains in the same range.



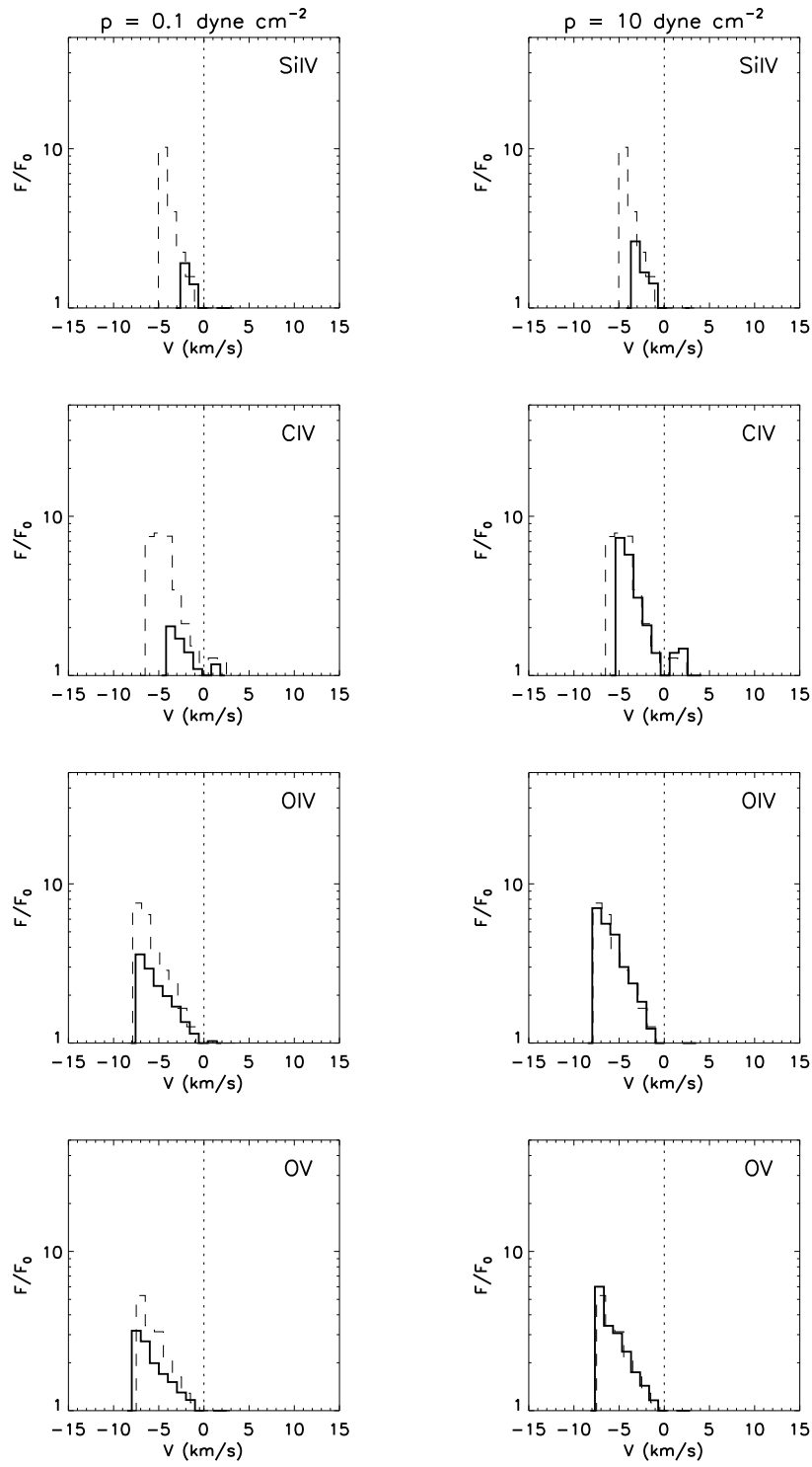


**Fig. 5.** Same as Fig. 2 for perturbations with different ambient pressures ( $p$ ) (cf. Sect. 3.1.4). The ratio  $R/h_0$  is unchanged with respect to the reference model.

lution of the perturbation is very fast: the plasma speed is everywhere  $< 3 \text{ km/s}$  already after 1 Sect. The plasma evolution does not differ significantly from that of the reference model; the maximum speed is practically the same, but the maximum density contrast is almost 50%

lower. As shown in Fig. 5, the flux distribution is quite similar to that of the reference model in the two oxygen lines. In the other two cooler lines, the maximum flux and speed are lower.

### 3.2. Global analysis of the parameter space

#### 3.2.1. The maximum density contrast and vertical downward speed

We now divide our models in three groups, one for each of the ambient pressures considered. This will be the basis of a general discussion on the parameter space. We will discuss our results in terms of  $R$  and  $\delta$ , since we have shown in Sect. 3.1 that the evolution of the perturbations at a given ambient pressure depends strongly on the initial radius and density contrast, and less on the temperature of the unperturbed medium.

Fig. 6a shows the contours of maximum density contrast in the  $\delta - R$  plane, together with the maximum downward speed<sup>2</sup>, reached during the evolution, for models with  $T_0 = 4.5 \cdot 10^5$  K and  $p = 3 \text{ dyn cm}^{-2}$ .

We find that the perturbations with the largest size and contrast evolve to very high density, and are therefore the most thermally unstable, independently of ambient pressure (cf. Fig. 6b). For  $p = 3 \text{ dyn cm}^{-2}$ , density contrasts starting from  $\delta < 1$  never grow above  $\delta_{max} = 10$ , for any perturbation size, confirming that only highly non-linear perturbations can become thermally unstable in these ambient conditions. Small perturbations ( $R < 2 \cdot 10^6$  cm) are remarkably stable, irrespective of  $\delta$ .

Large  $R$  and  $\delta$  (upper right of the figure) produce also high values of maximum downward speed, which however are always much smaller than the typical local sound speed ( $\sim 50$  km/s at  $T \sim 10^5$  K). High velocities (above 20 km/s) are reached also by very small and intense perturbations, in the region  $R \approx 10^6$  cm and  $2 < \delta < 3$ , i.e. in the lowest part of the figure, as a consequence of fast radial motions caused by the strong effect of thermal conduction at the beginning of the evolution of small perturbations ( $t \sim 0.1$  s).

For pressure  $p = 0.1 \text{ dyn cm}^{-2}$  and  $p = 10 \text{ dyn cm}^{-2}$  we find similar results, but for  $R$  approximately scaled to the respective thickness of the transition region. Results for  $p = 0.1 \text{ dyn cm}^{-2}$  are shown in Fig. 6b. We no longer find high speed values in the lower part of the figure because the lower boundary of  $R$  is comparatively larger than in Fig. 6a. Smaller values of  $\delta_{max}$  ( $\sim 1/6$ ) and higher values of maximum downward speed ( $\sim 40$  km/s) are reached, since the lower ambient density reduces the effect of the radiative cooling, but the thicker transition region leaves more space and time to let the gravity accelerate the perturbation.

For  $p = 10 \text{ dyn cm}^{-2}$ , the range of  $\delta_{max}$  is similar to that obtained for  $p = 3 \text{ dyn cm}^{-2}$ . The highest downward speed is reached by the largest perturbations ( $R \sim h_0$ ) in the range  $1 < \delta < 2$ , instead of  $\delta \sim 3$ .

We wish to point out, although with some caveats, that the results shown in Fig. 6a and 6b extend to atmospheres with thermal stratification previous work on the thermal stability of gravitationally stratified atmospheres (Malagoli et al. 1990, Reale et

al. 1991, RSP). The ambient conditions are in fact very different from those of the atmospheres without temperature stratification: now potentially unstable perturbations may not have enough time to collapse, before reaching the chromosphere where conditions are entirely different. To be more quantitative, we set a threshold value for  $\delta_{max} = 15$  above which we define a perturbation as thermally unstable, and then identify a boundary between thermal stability and instability in the  $\delta - R$  plane, which we approximate with a straight line as:

$$R = 1.2f - 0.25f^{-1}\delta \quad (4)$$

where a weak dependence on pressure  $f = 1 + 0.1 \log(p_0/p)$  is included, and where  $R$  is in units of  $h_0$  and  $p_0 = 3 \text{ dyn cm}^{-2}$ . The corresponding lines are shown as dashed lines in Fig. 6a and b. We note that the line shifts towards higher  $R$  and  $\delta$  in Fig. 6b, since the perturbations tend to be less thermally unstable with decreasing pressure.

As for the effect of the magnetic fields, in Fig. 6c we show results analogous to those in Fig. 6a, obtained in the assumption of purely one-dimensional evolution. The global trend is similar to those discussed above, but with minor differences: small and weak perturbations reach higher values of  $\delta_{max}$ , while the opposite occurs for large and intense perturbations. In other words it is easier to have unstable perturbations, but they do not fully develop to a very strong collapse. Higher downward speeds are reached.

#### 3.2.2. The line flux and effective speed distribution

We now discuss how the representative values of line flux and vertical effective speed synthesized from the models are distributed in the plane  $\delta - R$ . In Fig. 7, the vertical effective speed ( $v_F$ ) of the most intense line component, synthesized from the two-dimensional models at pressure  $p = 3 \text{ dyn cm}^{-2}$ , is shown in grey scales for each of the four UV lines (cf. Table 1). In the same pictures we show the contours of the maximum flux contrast  $F_{max}/F_0$  with respect to the static component. The comparison of the speed distribution with the flux distribution provides an indication of the strength of the Doppler shifts: vertical downward speeds, indicative of red-shifted components, are really important only if  $F_{max}/F_0 \gg 1$ , i.e. potentially detectable.

Fig. 7 shows that *the effective speeds of the most intense line components are largely downward speeds* in most of the explored parameter space, up to 11 km/s in Si IV line, not much lower in the other lines. Only results of C IV line are characterized by a small region of small upward  $v_F$  ( $\delta \sim 1$ ,  $R \leq 2 \cdot 10^6$  cm), with low  $F_{max}/F_0$  ( $\sim 1$ ). The highest values of  $F_{max}/F_0$  are different from line to line and are higher for cooler lines.

In Fig. 7, we note well defined regions of high downward  $v_F$  and high  $F_{max}/F_0$ . For the OV line the highest  $v_F$  is located in the region  $R \sim 4 \cdot 10^6$  cm and  $\delta \sim 1$ , i.e. in the region of the largest perturbations but not the most intense ones. This is also a region of high  $F_{max}/F_0$ , which extends farther to smaller perturbations ( $R \sim 3 \cdot 10^6$  cm). In the other lines both regions of

<sup>2</sup> The picture and the contour plot are obtained with an interpolation with quintic polynomials on the discrete and coarse grid of models shown in Table 1.

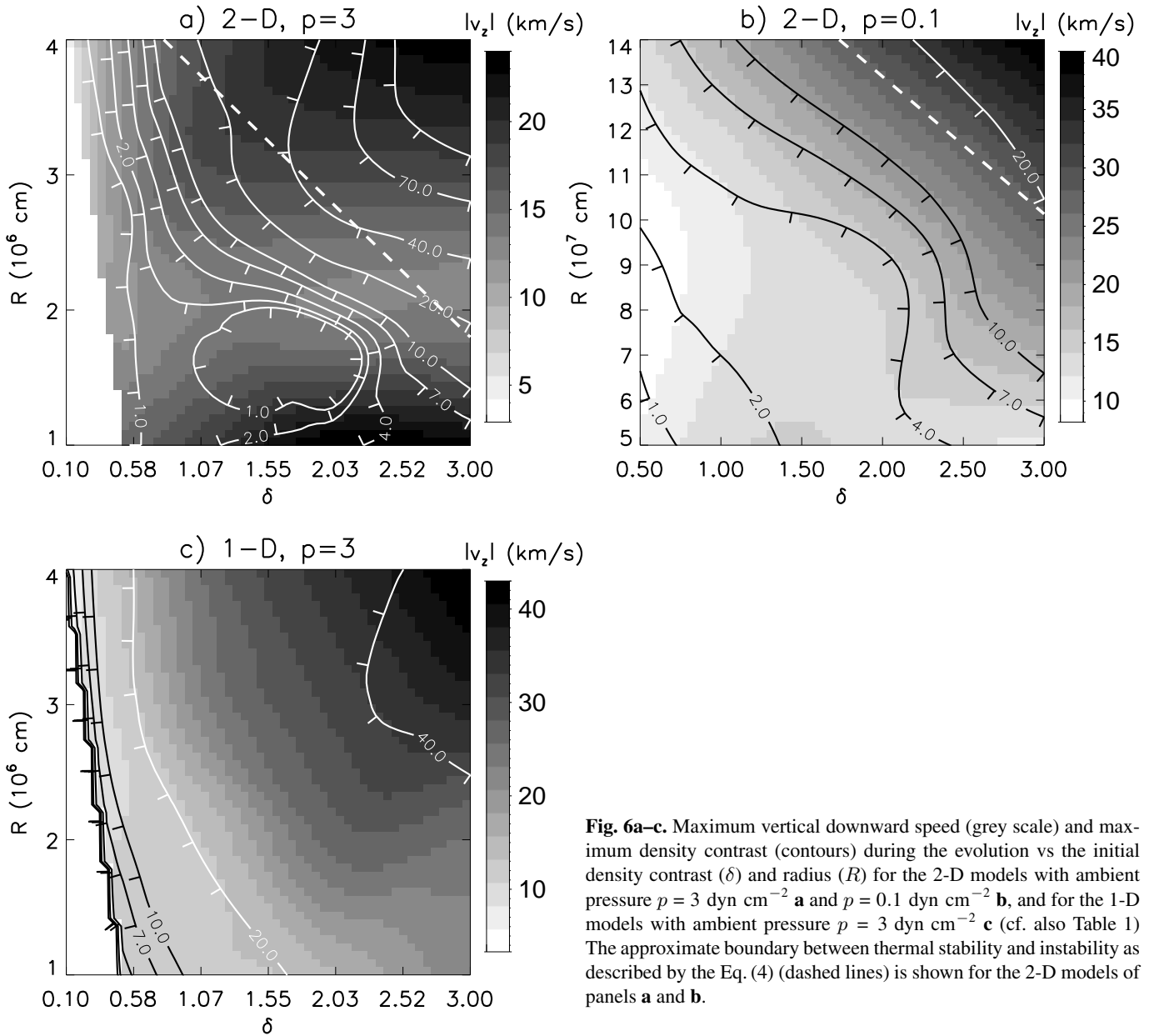


**Fig. 6a–c.** Maximum vertical downward speed (grey scale) and maximum density contrast (contours) during the evolution vs the initial density contrast ( $\delta$ ) and radius ( $R$ ) for the 2-D models with ambient pressure  $p = 3$  dyn cm $^{-2}$  **a** and  $p = 0.1$  dyn cm $^{-2}$  **b**, and for the 1-D models with ambient pressure  $p = 3$  dyn cm $^{-2}$  **c** (cf. also Table 1) The approximate boundary between thermal stability and instability as described by the Eq. (4) (dashed lines) is shown for the 2-D models of panels **a** and **b**.

high speed and flux contrast shift toward more intense perturbations: the cooler the line, the higher is  $\delta$ . In the OIV line, the highest speed and flux are both around  $R \sim 3 \cdot 10^6$  cm and  $\delta \sim 2$ . In the C IV line the maximum  $v_F$  is around  $2 < R < 3 \cdot 10^6$  cm and  $2 < \delta < 3$ , the maximum  $F_{max}/F_0$  at  $\delta \sim 3$ . In the Si IV line both maxima are close to the upper-right corner of the explored region ( $R \sim 4 \cdot 10^6$  cm,  $\delta \sim 3$ ). As already explained in Sect. 3.1.1, the reason for the shift toward more intense perturbations in cooler lines is that weak perturbations produce dense downflows at relatively high temperature, and therefore emit more effectively in the hotter lines. In any case *the regions of maximum  $v_F$  are also regions of high  $F_{max}/F_0$ .*

For the lower pressure  $p = 0.1$  dyn cm $^{-2}$  (Fig. 8) the maximum line flux is at downward effective speeds everywhere in the explored parameter space. The speeds are higher than those at  $p = 3$  dyn cm $^{-2}$  (up to 19 km/s in Si IV line), but  $F_{max}/F_0$  is

much lower. Again we find well defined regions of high speed, for very large perturbations ( $R \sim 1.4 \cdot 10^8$  cm), which are also regions of high line flux. Also at low pressure the location of the highest speeds moves toward weaker perturbations for hotter lines. We note that in the O V line the maximum flux contrast is everywhere very low ( $F_{max}/F_0 \leq 3$ ).

For  $p = 10$  dyn cm $^{-2}$  the results, including the values of flux contrast, are all very similar to those for  $p = 3$  dyn cm $^{-2}$ . As minor difference, we mention only that in the OIV line the highest speed is reached for slightly less intense perturbations ( $\delta \sim 1$ , instead of  $\delta \sim 2$ ).

We can now discuss the results obtained with purely one-dimensional hydrodynamics, shown in Fig. 9. The results do not change substantially: even the highest values of the downward speeds are similar to those reached with the 2-D description and, once again, we note the shift of the regions of maximum

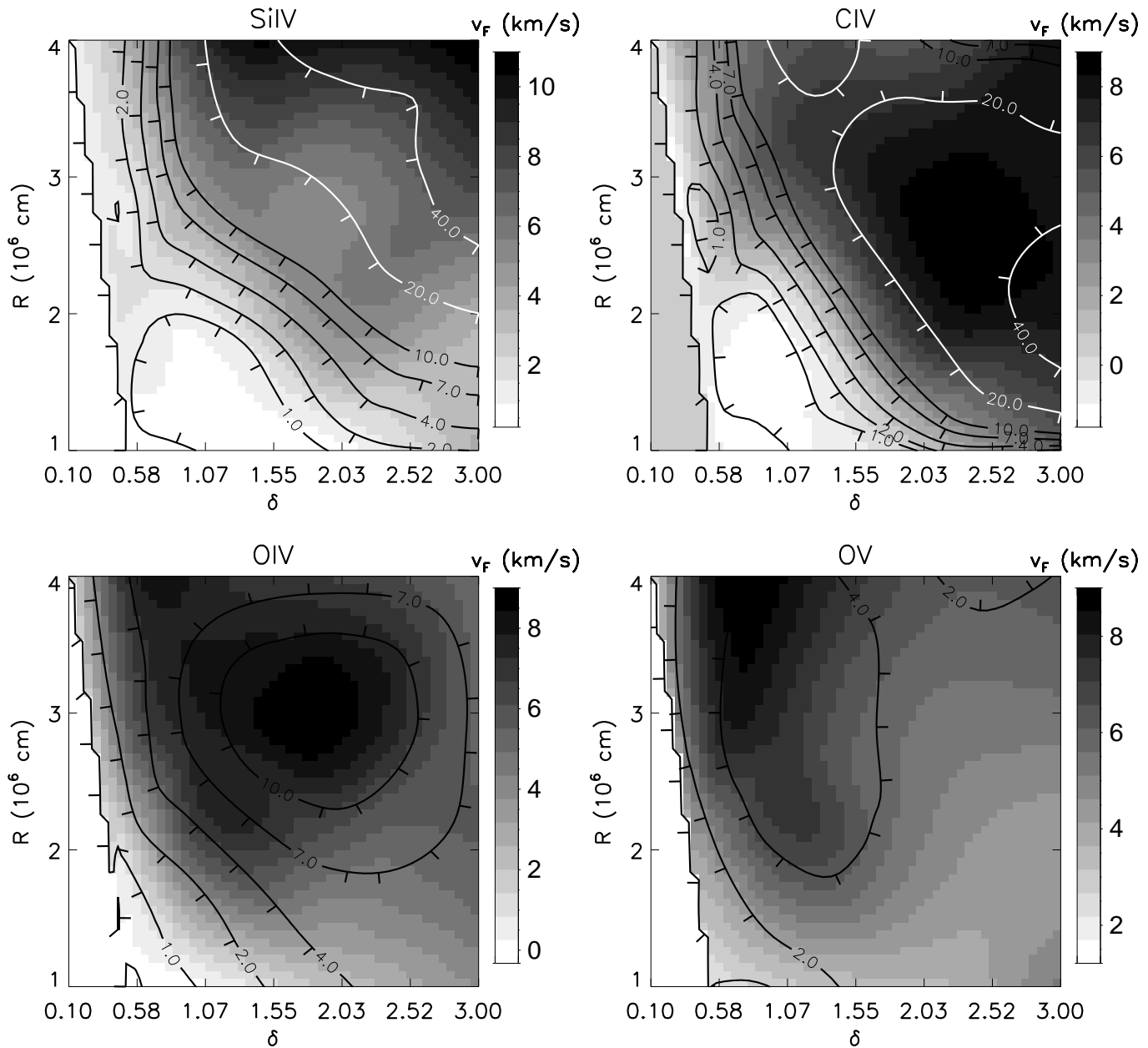


**Fig. 7.** Maximum effective vertical speed  $v_F$  (grey scales) and maximum flux contrast  $F_{max}/F_0$  (contours) for the four selected UV lines vs the initial density contrast ( $\delta$ ) and radius ( $R$ ) for the models with ambient pressure  $p = 3 \text{ dyn cm}^{-2}$  (cf. Table 1).

speed toward more intense perturbations for cooler lines. We find small regions of small upward maximum speed in the CIV and OV lines but at low flux. However, at variance from the 2-D models at the same pressure and more similar to the results found at lower pressure, the highest downward speed values are reached in all lines by the largest perturbations, and also the flux contrast is mostly much lower.

#### 4. Summary and conclusions

The reference model of Paper I has shown that an intense radiatively-cooling condensation in the solar transition region

can produce intense redshifted UV line emission at speeds comparable to those observed on the solar disk. In the present work we have explored the parameter space of the perturbations and examined which of them lead to intense redshifted emission.

The first step has been to study the effects and the physical implications of changing the control parameters one by one, finding that the parameters mainly governing the evolution and the line emission are the initial density contrast ( $\delta$ ) and the radius ( $R$ ) of the perturbation, whereas the ambient temperature ( $T_0$ ) is less important. The effect of ambient conditions in different regions of the solar atmosphere has also been explored by considering perturbations for different ambient pressure. In this

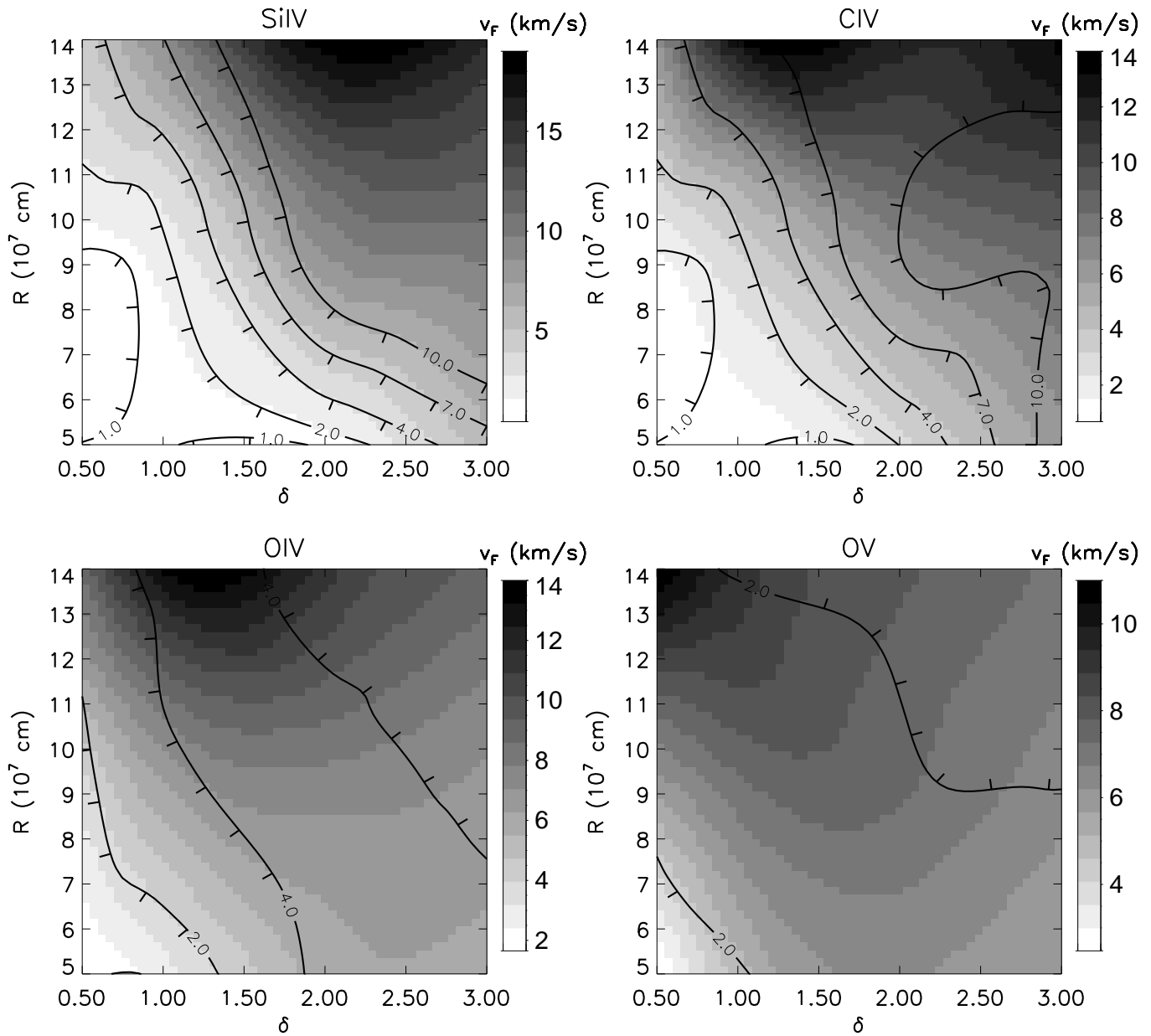


**Fig. 8.** Same as Fig. 7 for models with ambient pressure  $p = 0.1 \text{ dyn cm}^{-2}$ .

case the size of the perturbations has been scaled to the thickness of the transition region, since the thickness of the transition region depends on the ambient pressure. Pressure does not have much influence on the evolution, except for the time scales, which increase for decreasing pressure.

We have then studied our results in terms of  $R$  and  $\delta$ , for three values of pressure, and the global scenario they provide. The same has been done for a purely 1-D evolution, which mimics the effects of a strong magnetic field, for a pressure typical of active region loop ( $p = 3 \text{ dyn cm}^{-2}$ ).

One question is whether the perturbations are unstable, i.e. whether they collapse significantly. Care should be paid when comparing these results with those from previous work

on isothermal atmospheres (Malagoli et al. 1990, Reale et al. 1991, Reale et al. 1994), because our model conditions are very different: we consider a strong thermal stratification and a very dense chromosphere at the base of the transition region. As anticipated in Paper I, the present systematic study shows that only highly non-linear perturbations can evolve toward thermal instability, although the instability hardly develops fully before the blob falls onto the dense chromosphere; perturbations at low pressure are more thermally stable, while in 1-D geometry perturbations are unstable over a wider region of the  $\delta - R$  plane but do not reach high values of density contrast. The functional form (4) approximately describes the boundary between thermal stability and instability in the  $R - \delta$  plane.

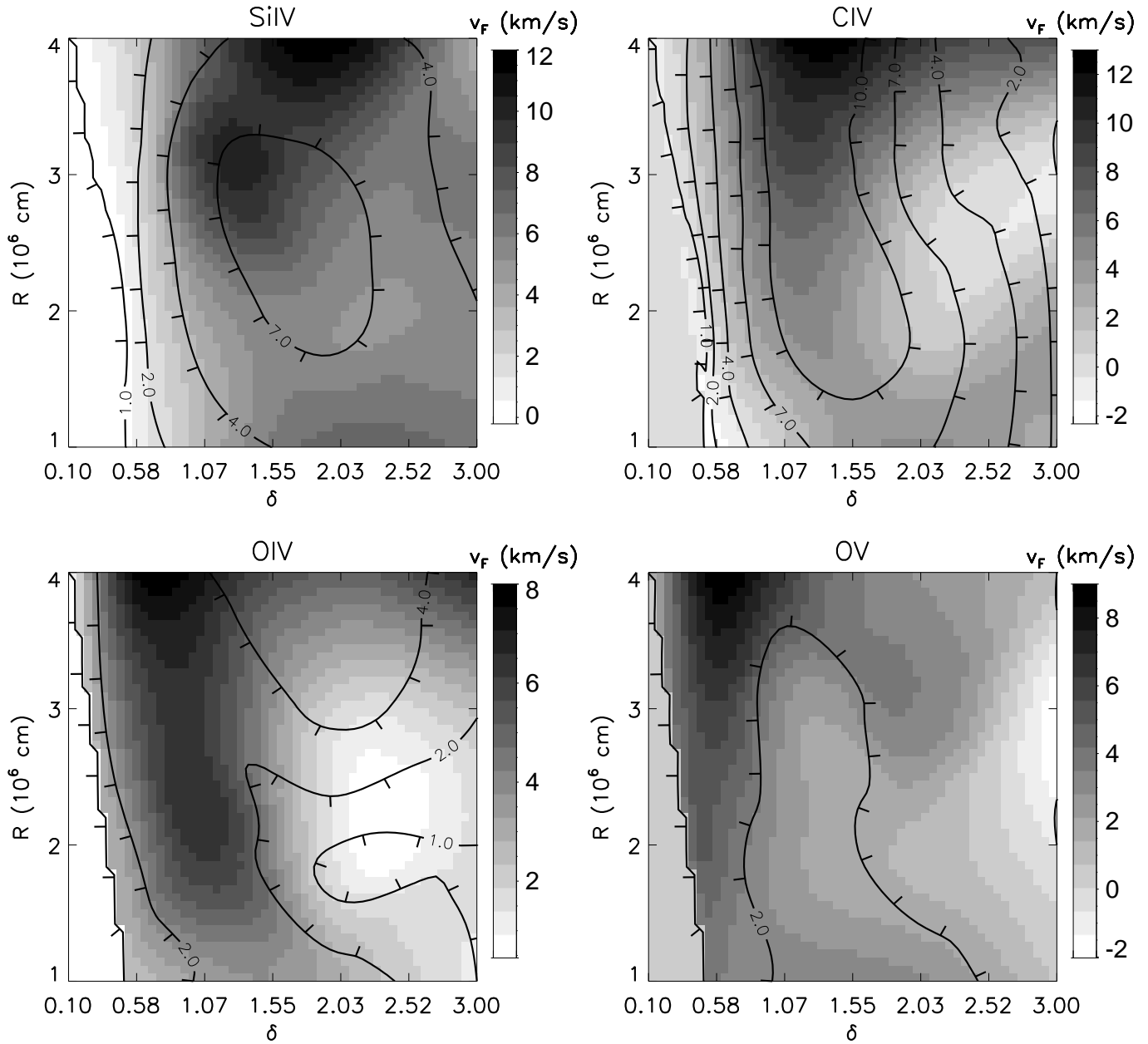


**Fig. 9.** Same as Fig. 7 for models with ambient pressure  $p = 3 \text{ dyn cm}^{-2}$  but with a purely 1-D evolution.

Our major interest is to derive information on the line emission and, in particular, on the presence of significant Doppler shifts. In the light of our ignorance of a realistic spectrum of possible perturbations, of their frequency of occurrence and of their filling factor, we cannot integrate properly the line emission over volume and time, as to compare our results directly to the observed line emission (which is typically integrated over instrumental spatial and temporal scales). Our choice, therefore, has been to identify the contribution of each perturbation in terms of line components at different Doppler shifts per unit time and unit area, so as to eliminate the role of the unknown distribution of perturbations. The distribution of the effective vertical speed

along the line of sight of the most intensely emitting line component, and its flux contrast above the static line component, can help to ascertain the presence of dominant Doppler-shifted components in the line emission and determine relevant ranges of expected speeds.

The results in Figs. 7–9 show that, over a wide range of the parameter space ( $\delta \geq 0.5$ ,  $R \leq h_0$ ), the evolution of condensations in the transition region can produce significant redshifted emission in the UV lines at speeds of several km/s, in particular for perturbations with i) a size of the order of the thickness of the transition region; ii) a strong initial density contrast; and iii)  $T_0$  above the line formation temperature. Furthermore, redshifts

are expected both in active and quiet solar regions, and have been found both with the fully 2-D model, and with the purely 1-D model, i.e. considering the effect of a strong magnetic field.

Although our analysis considers only the most luminous redshifted components, we can use the results shown in Figs. 7–9 to derive some general conclusions:

1. the generated redshifts are at speeds of the order of several km/s;
2. the maximum emission flux contrast  $F_{max}/F_0$  corresponds to redshifts above 8 km/s;
3. higher flux contrasts, especially in cooler lines, are obtained for high ambient pressures ( $p = 3 - 10 \text{ dyn cm}^{-2}$ , typical of solar active regions) rather than at low pressure (typical of quiet regions);
4. in the two Oxygen lines, formed at higher temperatures than the Si IV and C IV lines, the most conspicuous redshifts are produced by relatively weak perturbations (density contrast  $\delta < 2$ ), probably more easily triggered;
5. the highest flux contrast correlates with the highest Doppler shift velocity of the most intense flux component ( $v_F$ ), at any pressure;
6. 1-D modeling does not yield qualitatively different results, but produces higher redshift speeds in the cooler lines and lower  $F_{max}/F_0$  (a factor 2-10) in all lines.

A detailed comparison with observations is beyond the scope of this paper, but we note that: i) the observed redshifts are in the range of those found here, although higher values have also been detected (Achour et al. 1995); ii) active regions and oxygen lines usually show redshifts higher than quiet regions and other lines, respectively (Brekke 1993, Achour et al. 1995), in qualitative agreement with points (3) and (4) above.

The study of the parameter space has shown that the emission of luminous redshifted components in UV lines caused by radiatively-driven downflows may be a common effect both in solar active regions and in quiet regions. The scenario that we propose, i.e. redshifts as signature of downdrafts driven by thermal instability, still deserves further investigation. The synthesis of line profiles integrated over specific volumes and times should allow us to constrain the spectrum, repetition time and filling factor of the perturbations, and, in turn, to investigate how such perturbations are formed. In particular we should be able to ascertain how the perturbation spectrum compares, for instance, with the spectrum of possible non-linear MHD waves which may trigger them. Also the effects of non-equilibrium ionization deserve further studies. Finally such scenario could be extended also to other stars, characterized by ambient conditions different from those on the Sun.

*Acknowledgements.* We thank S. Sciortino, R. Pallavicini and the referee for useful comments. We acknowledge partial support from Ministero dell'Università e della Ricerca Scientifica e Tecnologica, Agenzia Spaziale Italiana and Consiglio Nazionale delle Ricerche.

## References

- Achour H., Brekke P., Kjeldseth-Moe O., Maltby P., 1995, ApJ, 453, 945.
- Brekke P., 1993, ApJ, 408, 735.
- Brekke P., 1994, Space Science Reviews, 70, 97.
- Hansteen V., 1993, ApJ, 402, 741.
- Hansteen V., Maltby P., Malagoli A., 1996, proceedings of Yohkoh Conference "Observations of Magnetic Reconnection in the Solar Atmosphere", Bath, March 20-22, 1996, in press.
- Landini M., Monsignori Fossi B. C., 1990, A&AS, 82, 229.
- Malagoli A., Rosner R., Fryxell B., 1990, MNRAS, 247, 367.
- Reale F., 1995, Comp. Phys. Comm., 86, 13.
- Reale F., Peres G., Serio S., 1996, A & A, in press (Paper I).
- Reale F., Rosner R., Malagoli A., Peres G., Serio S., 1991, MNRAS, 251, 379.
- Reale F., Serio S., Peres G., 1994, ApJ, 433, 811 (RSP).
- Serio S., Peres G., Vaiana G. S., Golub L., Rosner R., 1981, ApJ 243, 288.